Solar Energy 212 (2020) 275–281

Contents lists available at ScienceDirect

Solar Energy

journal homepage: www.elsevier.com/locate/solener

Low-voltage room-temperature electrochemical deposition of perovskite films for solar cell devices

Deye Liu, Kunpeng Liu, Yueying Liu, Jihao Bai, Meng Dai, Fengmin Liu *, Geyu Lu

State Key Laboratory of Integrated Optoelectronics, College of Electronic Science and Engineering, Jilin University, 2699 Qianjin Street, Changchun 130012, China

ARTICLE INFO

Keywords:
Perovskite solar cell
Electrochemical deposition
Low voltage

ABSTRACT

A uniform $CH_3NH_3PbI_3$ layer was successfully deposited on a mesoporous TiO_2 layer (mp-TiO_2) via a two-step low-voltage room-temperature electrochemical deposition method without annealing. The deposited perovskite crystals were applied to cover a surface mp-TiO_2 electron transport material and fill the nanoscale blank of mp-TiO_2. A mesoporous electron transport material and a platinum sheet were used as working and counter electrodes, respectively. The obtained film was then utilized to fabricate a mesoporous hybrid perovskite solar cell (PSC) with the configuration of a fluorine-doped tin oxide/compact TiO_2/mp-TiO_2/perovskite/Spiro-OMeTAD/Au electrode. An efficiency of 15% was achieved by adjusting Pb and MAI deposition and by using champion cells with an active area of 2 mm × 2 mm at 1 sun under an AM 1.5 condition. The perovskite layers and PSCs were analyzed through several characterization methods. Results demonstrated that this deposition technology could be applied to easily control the morphological characteristics of perovskite layers. Thus, a high power conversion efficiency was obtained. This study proposed a possible perovskite deposition process and demonstrated that electrochemical deposition could have potential for application in PSC fabrication.

1. Introduction

Perovskite solar cells (PSCs) have been widely explored because of a remarkable increase in their efficiency. In 2009, Kojima et al. published the first article about PSCs and achieved an efficiency of 3.8%. In 2019, Seok et al. proposed that PSCs' efficiency is 24.2%, which is equivalent to about a sixfold increase (National Renewable Energy Laboratory, 2020). Typically, a PSC device is composed of five different layers: an electric transparent glass substrate, an electron transport layer, a perovskite light absorption layer, a hole transport layer (HTL), and an electrode (Kim et al., 2014; Correa-Baena et al., 2017). Among them, the perovskite absorption layer is the most significant part, where photons are converted to excitons (Zhao and Zhu, 2014). Perovskite materials usually mean a group of materials with an ABX_3-type molecular structure. In the solar cell field, it represents methylammonium lead iodide ($CH_3NH_3PbI_3$, $MAPbI_3$ briefly) in most instances (Tai et al., 2019; Chen et al., 2019; Zimmermann et al., 2018; Chen et al., 2018). $MAPbI_3$ has a series of outstanding photovoltaic properties, high charge mobility, diffusion length, adjustable band gaps, high light absorption, and so on (Huang et al., 2017). Numerous ways of $MAPbI_3$ film deposition have been developed to take advantage of these properties and improve device performance (Shin et al., 2017; Qiu et al., 2017; Tan et al., 2017). Most studies have focused on making high-quality $MAPbI_3$ films via spin coating technology (Zhou et al., 2017). This technology can be applied to fabricate high-quality cells, but it still has some drawbacks, such as needing an antisolvent washing process and performing poorly in large cell manufacturing (Liu et al., 2019). Another widely used method of PSC fabrication is thermal evaporation, which is known as a scalable means with an efficient thickness control method; however, it requires high temperature and high vacuum (Wang et al., 2018), consequently increasing the costs of PSC mass production. Therefore, other ways should be developed to manufacture high-quality $MAPbI_3$ films.

A $MAPbI_3$ film should be compact and homogeneous to reduce energy wastage and maintain the high efficiency of PSCs (Lee et al., 2017; Bi et al., 2016). Hence, the deposition technologies of $MAPbI_3$ films must be controllable and adjustable. Furthermore, the speed of deposition should be fast, considering that $MAPbI_3$ materials are unstable in ambient air. A shorter deposition process can reduce the possibility of the unexpected exposure of $MAPbI_3$ and prevent disintegration (Han et al., 2015; Jeon et al., 2018; Yi et al., 2016). As a classical technology, electrochemical deposition has been proven to have many advantages in the preparation of perovskite. Firstly, in commercial production, the

* Corresponding author.
E-mail address: liufm@jlu.edu.cn (F. Liu).

https://doi.org/10.1016/j.solener.2020.11.010
Received 25 April 2020; Received in revised form 29 October 2020; Accepted 4 November 2020
Available online 24 November 2020

preparation of perovskite by electrodeposition theoretically does not waste the toxic leaded electrodeposition solution. Because the solution can be reused by adding lead salt (Charles et al., 2018). Secondly, compared with spin coating method, almost all conductive substrates of any shape can be used as substrates for perovskite deposition, which means that electrodeposition is a very competitive method for the preparation of tandem cells and flexible cells (Lee et al., 2019). Last but not least, electrodeposition is not only a scalable deposition technology, but also a highly controlled technology. By adjusting the deposition time, concentration or current, the thickness of the deposited film can be effectively controlled. In the past two years, literature has shown that for the perovskite prepared by electrodeposition, even though the thickness reaches the micron level, far exceeding the thickness requirement of the general PSCs for the absorptive layer, the perovskite still performs well in the morphology (Tang et al., 2019).

Furthermore, some previous work has shown that it is feasible to prepare PCSs by electrodeposition. In 2015, Chen et al. deposited a MAPbI3 film on substrates through a three-step electrochemical deposition technology and fabricated a mesoporous PSC device that exhibits an efficiency of 10.19%. In addition, they also prepared PSC with active area of 4 cm2 in the same way and obtained an efficiency of 4.47%. However, hydroiodic acid is needed to iodinate PbO into PbI2 in their three-step synthetic route, but a long immersion period (about 2 h) in a methylammonium iodide (CH3NH3I, MAI for short) solution and a heating process (100 °C, 15 min) are also required. Adding HI increased complexity and danger of the experiment. In the same year, Cui designed another set of deposition processes, changing the intermediate product of perovskite deposition from PbO2 to PbO, and using I2 vapor to replace HI, reducing the risk of reaction. Meanwhile, the efficiency of PSCs prepared by electrochemical deposition was improved to 12.5%. In 2016, Popov and his colleagues studied the relationship between electrodeposition solution system, deposition time and product perovskite film thickness while preparing large-size perovskite solar cells using electrochemical deposition. In 2017, Zhou et al. simplified the electrochemical process and developed a two-step electrochemical deposition technology that is slightly similar to a traditional two-step spin coating method; however, they introduced a high voltage pulse (−20 V, 1 s). The prepared cell is a typical planar device, which is inferior to mesoporous devices in terms of efficiency (Zhao and Zhu, 2014). Because the mesoporous PSCs tend to have larger interfacial contact area, shorter carrier transport path and longer optical transport path.

In this work, perovskite was electrochemically deposited on a mesoporous TiO_2 layer (mp-TiO_2) through a two-step electrochemical deposition technology, and a champion mesoporous PSC device with an efficiency of 15% was fabricated by optimizing experimental conditions.

2. Experimental section

2.1. Materials

All materials were purchased from Aladdin Industrial Corporation and had a purity of over 99% unless stated otherwise.

2.2. Preparation of TiO_2 layers via spin coating

mp-TiO_2 was prepared in accordance with previously described methods (Zhou et al., 2015; Liu et al., 2019). An etched fluorine-doped tin oxide (FTO; Nippon Sheet Glass Company) glass with a sheet resistance of 14 Ω/sq was cleaned by ultrasonicating in detergent, DI water, acetone, and isopropanol for 15 min. The substrate was treated with oxygen plasma for 10 min. A compact TiO_2 layer was deposited on the FTO substrate by spin coating twice with a precursor solution containing 10% (v/v) titanium diisopropoxide bis(acetylacetonate; 75 wt% in 2-propanol) in 1-butanol at 2000 rpm for 30 s. Then, the layer was heated on a hotplate at 150 °C for 20 min. mp-TiO_2 was formed by spin coating a precursor solution prepared by diluting 1 g of 18NR-T TiO_2 paste (Polymer Light Technology Corporation) in 7 g of ethyl alcohol (≥99.7%, Beijing Chemical Works) at 5000 rpm for 30 s. The substrate was annealed at 450 °C for 30 min. The sample was named mp-TiO_2 substrate.

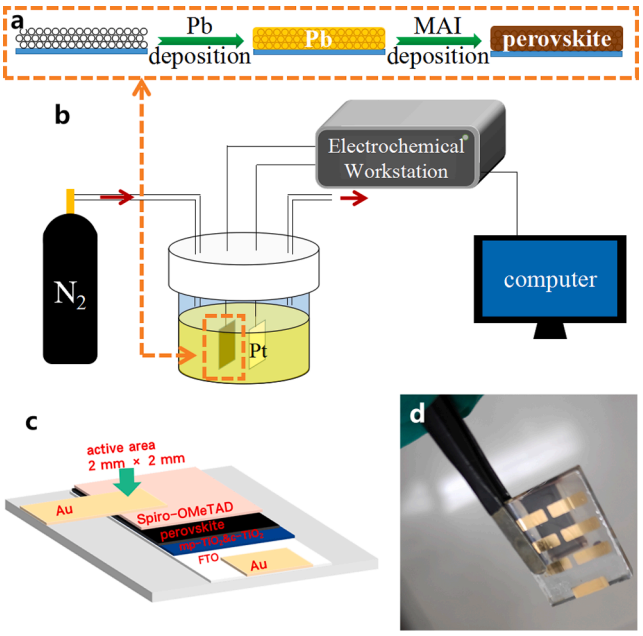

Fig. 1. Schematic of perovskite synthesis (a), experimental system (b) and device structure (c), along with picture of prepared device (d).

2.3. Preparation of a Pb layer via electrodeposition

The electrochemical deposition of a Pb layer was carried out in a nitrogen-protected two-electrode cell controlled by an electrochemical station (CHI760E, CH Instruments Incorporation; Fig. 1). A platinum sheet and a mp-TiO_2 substrate prepared previously were used as a counter electrode and a working electrode, respectively. The deposition bath was a solution of 10 mM PbI_2 (99.99%, Polymer Light Technology Corporation), 1.3 M NaI, and 0.7 M ethylene glycol tertiary butylether dissolved in dimethyl sulfoxide. Deposition was performed at a constant applied potential difference of −2 V for 240, 260, 280, and 300 s, respectively. The samples were washed with ethyl alcohol and dried with N_2 flow.

It should be noted that although it has been reported in the previous literature that the application of transient high bias can optimize the product lead layer (Zhou et al., 2017). However, the Pb nuclei is harmful to the bottom-up deposition of Pb, and prevents Pb from entering the mesoporous layer. In our early experiments, both the high voltage pulse and deposition voltage higher than 2 V can caused the Pb layer fall off (Fig. S1).

2.4. Preparation of $MAPbI_3$ via electrodeposition

$MAPbI_3$ was in situ prepared by depositing MAI (99.99%, Polymer Light Technology Corporation) onto the as-prepared Pb layer. The reaction was performed in a 10 mg/mL MAI solution in isopropanol. A square-wave pulse potential difference (f = 5 Hz) was introduced with a +2 V first half-wave amplitude and a −2 V second half-wave amplitude to carry out electrodeposition. Deposition was separately carried out for 120, 140, 160, and 180 s. All the other reaction conditions were the same as Pb deposition.

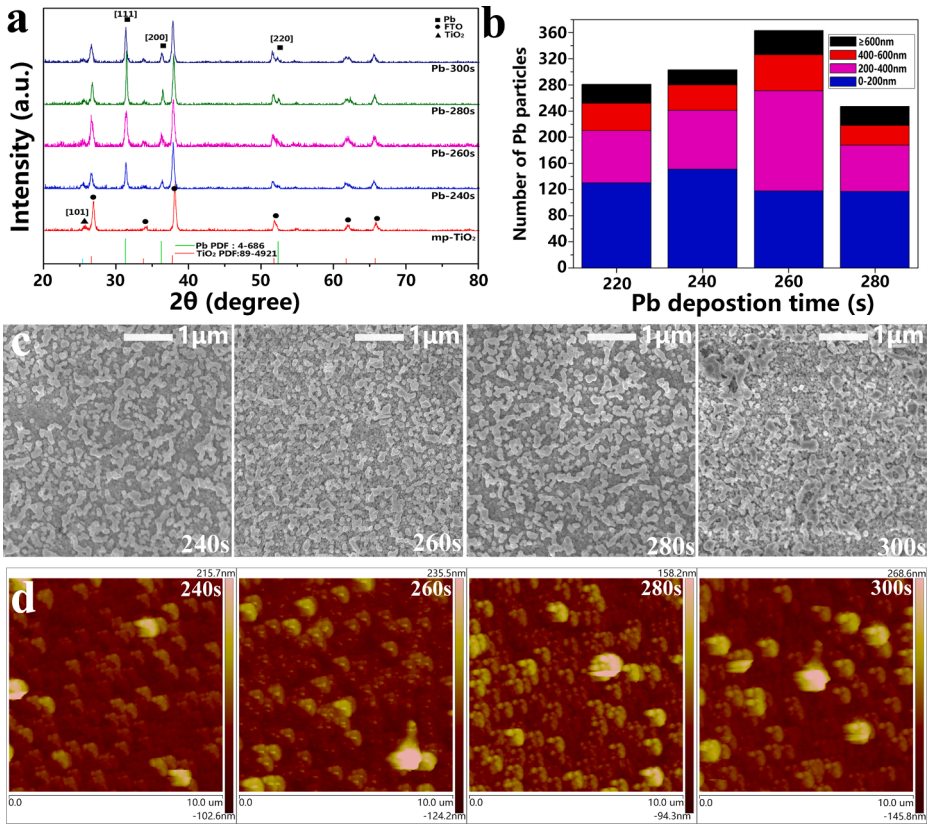

Fig. 2. Characteristics of Pb layers with different Pb deposition times. a) XRD results; ●, ▲, and ■ are used to indicate the XRD peaks of the FTO substrate, the TiO2 layer, and the Pb layer, respectively. b) Statistics of surface pb particle size and number of samples with different Pb deposition time, which is approximately 4.5 μm × 4.5 μm. c) SEM images. d) AFM images.

2.5. Fabrication of PSCs

About 40 μL of 2,2′,7,7′-tetrakis(N,N-di-*p*-methoxyphenylamine)-9,9-spirobifluorene (Spiro-OMeTAD, 99.99%, Polymer Light Technology Corporation) precursor solution was spin coated on the prepared $MAPbI_3$ film at a speed of 2000 rpm for 60 s in a glovebox and then aged in dry air for 20 h to form HTL. The spiro-OMeTAD precursor was prepared via a typical reaction, and 40 mg of spiro-OMeTAD was dissolved in 1 mL of chlorobenzene. Then, 16 μL of 4-*tert*-butylpyridine and 33 μL of lithium bis(trifluoromethanesulfonyl)imide (Li-TFSI, 99.99%, Polymer Light Technology Corporation) solution (175.1 mg of LI-TSFI in 1 mL of acetonitrile) were added. Lastly, 100 nm of Au (≥99.99%) was thermally evaporated on top of HTL in vacuum as the upper electrode of the solar cell. The size of sample glass used is 1.5 cm^2, and the active area of PSCs was 4 mm^2 controlled by a shadow mask (Fig. 1c).

2.6. Characterizations

The phase and crystallinity of the as-prepared samples were identified through X-ray diffraction (XRD) by using a Rigaku D/max-2500 diffractometer with Cu-Kα radiation at a wavelength of 1.5406 Å, and the corresponding data were collected at 40 kV in the range of 20°–80° (2θ). The morphological characteristics of the samples were observed under a scanning electron microscope (SEM, JEOL JSM-7500F) and an atomic force microscope (AFM, Icon, Veeko). Current–voltage (J–V) curves were measured with a Keithly 2400 source meter under 1 sun illumination (100 mW/cm^2, AM 1.5) from a parallel light source system (CHF-XM35-500 W, Beijing Changtuo) equipped with a 500 W xenon lamp. Electrochemistry impedance spectra (EIS) were obtained using an *Autolab 302B*, where the bias voltage was 0.9 V. A small voltage perturbation of 20 mV was applied during the measurement at a frequency range of 1 MHz to 0.1 Hz. The measured data were fitted using Z-View.

3. Results and discussion

3.1. Characteristics of Pb layers

The samples were initially characterized through XRD to preliminarily confirm the Pb layers' coverage. The XRD patterns of the mp-TiO_2 substrate and the prepared Pb layers are shown in Fig. 2a. The XRD results of the Pb deposition products are similar to the peaks of pure Pb (card no. 4–686) in the [1 1 1], [2 0 0], and [2 2 0] directions. Moreover, the Pb peaks of 260 s sample are sharper than the others. This finding indicates that the 260 s sample may be the best covered among the samples (Bunaciu et al., 2015). The peaks of mp-TiO_2 can be found in the XRD spectrum because deposited Pb layers are much thinner than mp-TiO_2 layers.

SEM was used to observe the morphological characteristics of the deposited Pb layers and investigate Pb layer deposition. The SEM images of the Pb samples with different deposition times (Fig. 2c) show that Pb exists as irregular particles on the mp-TiO_2 surface. Meanwhile, the coverage of these Pb particles is highly related to Pb deposition time due to the changes in their number and size (Fig. 2b). To better visualize the variation of the size and number of lead particles on the surface of different samples, we counted the number of particles with different size on the surface of the sample in SEM images the size and number of lead particles on different samples (Fig. 2b).

The 240 s Pb layer has a poor Pb particle coverage, suggesting that 240 s is too short to complete the deposition of an ideal Pb layer. When Pb deposition occurs for more than 280 s, Pb particles tend to agglomerate. This agglomeration can severely injure the coverage and

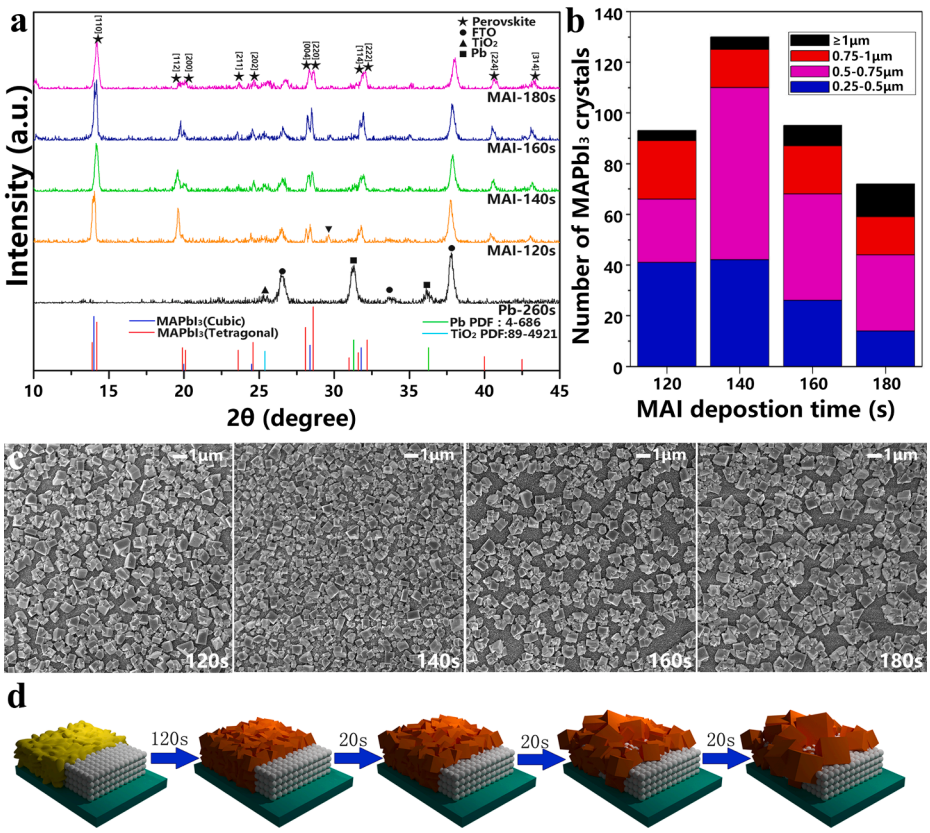

Fig. 3. Characteristics of MAPbI3 layers with different MAI deposition times and with a Pb deposition time of 260 s. a) XRD results; ■, ★, ▲, and ● represent the peaks of the Pb layer, the perovskite layer, TiO2, and the FTO substrate, respectively. b) Statistics of surface pb particle size and number of samples with different lead deposition time.Statistics are based on the part of SEM image in Fig. 3B, which is approximately 7 μm × 7 μm. The change in sampling area is due to the larger volume of perovskite compared to lead particles. c) SEM characterizations. d) Schematic of the sample's variation with an increase in MAI deposition time.

smoothness of Pb particle layers. Therefore, 260 and 280 s can be accepted as appropriate deposition times.

AFM was selected to expose the roughness of the Pb layers' surface and to further optimize Pb deposition time. The AFM images (Fig. 2c) reveal that the uniformity of Pb particles reduces as the deposition time is prolonged because new Pb particles keep taking shape while the existent Pb particles grow. Hence, a shorter deposition time is beneficial to Pb particle homogeneity, which makes 260 s a better option than 280 s.

3.2. Characteristics of perovskite layers

All the perovskite layers were synthesized on the basis of 260 s Pb layers. In comparison with the sample without MAI deposition, the synthesized perovskite sample has no Pb peaks, as shown in the XRD results (Fig. 3a). Conversely, the peaks of perovskite appear in the [200], [202], [220], [310], [224], and [314] directions, and this observation is the same as that described in other studies, indicating that Pb particles are fully transformed into perovskite (Zhou et al., 2017). Few unmatched peaks indicated by ▼ are presented in the XRD patterns of the perovskite sample, and such peaks may arise from the slight decomposition of the $MAPbI_3$ sample. Compared with the literature (Zhou et al., 2017), the optimized Pb layer deposited on the mesoporous surface in our study was much thinner (about 30 nm to 40 nm, as shown in Fig. S2) with a lower coverage rate, and MAI deposition time was almost the same. So, the unconverted lead is unlikely to exist.

By comparing the SEM images of samples before (Fig. 2c) and after conversion (Fig. 3c), it can be found that the size of perovskite on the surface is far larger than that of lead particles on the surface, even considering the volume expansion during the conversion process from lead to perovskite. This may be due to the limitation of space in the mesoporous layer, so that part of Pb2+ converted from Pb can only combine with MA+ and I− to form perovskite on the surface. In order to quantify and plot the change coverage, The size and number of perovskite crystals on the surface of the sample were also counted (Fig. 3b). The SEM images (Fig. 3b) also show that the coverage of perovskite films also increases initially from 120 s to 140 s and decreases thereafter (from 140 s to 180 s). This increase in coverage may be simply triggered by an increase in the in situ synthesized perovskite crystals, and the decrease in coverage probably results from the alternating voltage bias. During MAI deposition, the positive bias turns Pb into Pb^{2+}, and I^- accumulates from the MAI solution and moves to the working electrode. Meanwhile, the negative bias causes MA^+ to become Pb^{2+} and I^- alongside the working electrode to form a perovskite layer. In this process, perovskite crystals may dissolve in the solution. Large Pb particles more likely form large perovskite crystals. Therefore, as the MAI deposition time is prolonged, small perovskite crystals initially decompose and then recrystallize on large perovskite crystals. As a result, the perovskite coverage on the mp-TiO_2 substrate decreases as the size of crystals increases.

To show the changes in surface MAPbI3 size and coverage, we used a lower magnification factor than the lead sample when comparing samples with different MAI deposition times. In view of the need to compare SEM images before and after conversion, the SEM images of samples with different Pb deposition times before (Fig. S3a-d) and after (Fig. S3e-h) 140 s MAI deposition with the same magnification were given in the supporting information. It can be seen that the surface perovskite coverage rate is approximately similar to the lead layer under the condition that MAI deposition time is the same.

In order to determine whether the annealing process is necessary, an optimized perovskite sample was annealed at 100 °C for 15 min under nitrogen environment. SEM images of samples before and after annealing (Fig. S4) show that there is no obvious change in crystallinity after annealing. Meaning that annealing is not essential, which is consistent with the results reported in the previous literature.

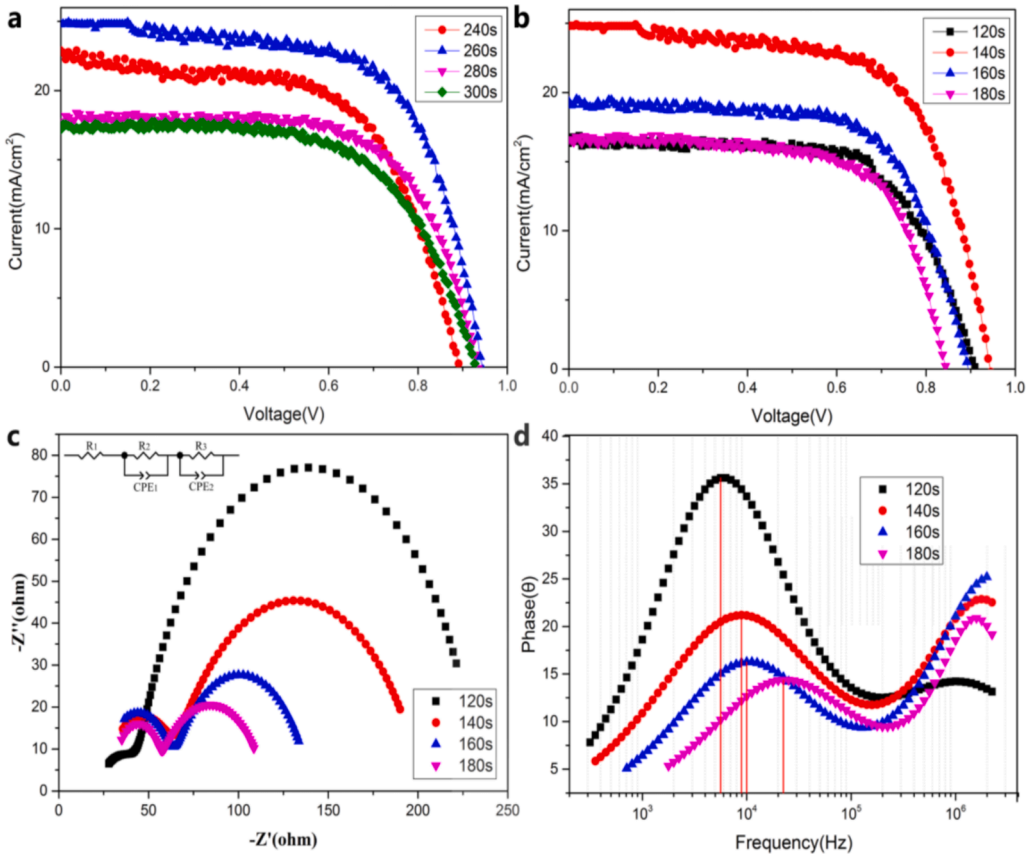

Fig. 4. Device performance of fabricated cells. a) J–V curves of the devices with different Pb deposition times and with an MAI deposition time of 140 s. b) J–V curves of devices with different MAI deposition times and with a Pb deposition time of 260 s. c) Nyquist plots (the equivalent circuit is exhibited in its top left corner) and d) bode plots from the EIS measurements of the samples with different MAI deposition times.

Table 1
Performance of PSCs with different Pb deposition times with an MAI deposition time of 140 s.

Pb deposition time (s)	MAI deposition time (s)	Jsc (mA/cm^2)	Voc (V)	FF (%)	PCE (%)
240	140	20.17 ± 2.58	0.91 ± 0.05	64.76 ± 5.00	11.79 ± 1.03
260	140	23.24 ± 2.04	0.92 ± 0.04	66.63 ± 4.01	14.33 ± 1.15
280	140	17.80 ± 0.48	0.93 ± 0.01	68.69 ± 3.39	11.41 ± 0.97
300	140	18.08 ± 1.21	0.93 ± 0.03	65.17 ± 2.45	10.92 ± 0.71

Table 2
Performance of PSCs with different MAI deposition times and with a Pb deposition time of 260 s.

Pb deposition time (s)	MAI deposition time (s)	Jsc (mA/cm2)	Voc (V)	FF (%)	PCE (%)
260	120	17.63 ± 0.66	0.90 ± 0.01	68.55 ± 0.67	10.84 ± 0.39
260	140	23.24 ± 2.04	0.92 ± 0.04	66.63 ± 4.01	14.33 ± 1.15
260	160	19.05 ± 0.81	0.92 ± 0.04	61.00 ± 7.23	10.75 ± 0.8
260	180	16.24 ± 0.05	0.85 ± 0.01	63.33 ± 5.06	8.75 ± 0.59

3.3. Device performance

The device configuration of FTO/c-TiO_2/mp-TiO_2/electrodeposited perovskite/Spiro-OMeTAD/Au was chosen to fabricate the PSCs for device characterization. All the studied PSCs were measured at 1 sun intensity (100 mW/cm^2) under the simulated AM 1.5 illumination.

A 140 s MAI deposition was executed on 240 s, 260 s, 280 s, and 300 s Pb layers to synthesize a perovskite absorption layer, fabricate cells, and investigate the effect of Pb deposition time on device performance. The J–V curves of the prepared devices are presented in Fig. 4 a. All the detailed J–V data of the champion devices among them are recorded in Table 1.

In different phases of Pb deposition, deposition time affects different photovoltaic parameters. When deposition time is less than 260 s, the open circuit voltage (V_{oc}) and photoelectric conversion efficiency (PCE) increase significantly as the Pb deposition time is prolonged. Considering that Pb deposition time mainly influences the coverage of Pb particles on mp-TiO_2 substrates during this phase, we can conclude that a Pb layer with a high particle coverage can easily form a well-covered perovskite layer, which has a low rate of carrier recombination (Zhou et al., 2014; Quilettes et al., 2015).

Conversely, when the Pb deposition time is over 260 s, the short circuit current density (J_{sc}) and PCE of the device decrease dramatically possibly because the Pb particle size homogeneity decreases due to an excessive Pb deposition time. Inhomogeneous Pb particle size likely breaks down the uniformity of the synthesized perovskite layers, damages the hole transport layer deposited on the perovskite-absorbed layer, and impedes carrier transport.

The perovskite layers with 260 s Pb deposition and different MAI deposition times (120, 140, 160, and 180 s) were prepared for device fabrication and characterization. Their detailed J–V data can be found in Table 2.

Table 3
Interface resistance and electrons lifetime of PSCs with different MAI deposition time.

MAI deposition time (s)	R1 (Ω)	R2 (Ω)	R3 (Ω)	electrons lifetime (s)
120	25	20	160	2.83×10^{-5}
140	35	45	130	1.79×10^{-5}
160	30	40	70	1.59×10^{-5}
180	30	35	55	7.11×10^{-6}

The J–V curves of these solar cells show that J_{sc}, V_{oc}, and PCE of the devices increase with deposition with an MAI deposition time of less than 140 s. However, when the deposition time exceeds 140 s, the parameters show an opposite trend. Consistent with the analysis of perovskite layers, this result indicates that 140 s is the most suitable deposition time for MAI deposition.

The abnormal filling factor (FF) of the devices with 180 s of MAI deposition increases mainly because of a remarkable decrease in V_{oc} and J_{sc} of the devices, so FF cannot be used as a factor to evaluate cell performance.

Devices are characterized through EIS measurements to further explore the relationship between MAI deposition time and device performance (Yi et al., 2014; Guerrero et al., 2016; Pockett et al., 2015). The Nyquist plots and bode plots are shown in Fig. 4c and d. After the comparison of the impedance spectra and the cell structure, three primary resistances can be found in the device at the interface among c-TiO_2, mp-TiO_2, perovskite, and HTL denoted as R_1, R_2, and R_3, (Table 3).

R_1 and R_2 of different devices are basically equal except R_2 of the MAI-120 s device, which is much smaller than that of the others. This result is caused by small Pb particles remaining among the mp-TiO_2 layer. R_3 of these cells tends to reduce as the MAI deposition time is prolonged possibly because of the incresae in the sizes of perovskite crystals, which expand the contact area of perovskite and HTL, decrease the probability of carrier recombination at the grain boundary, and weaken the resistance of devices.

From the bode plots of EIS-characterized devices, the electron lifetime (τ_e) can be figured out. The longer MAI deposition time attracts shorter τ_e. This phenomenon is probably associated with the coverage and homogeneous decrease in the perovskite layer during MAI deposition. A perovskite layer with low coverage and poor homogeneity introduces extra defects and traps and shortens the carrier lifetime.

Considering the discussion about EIS characterization, we can assume that the increase and decrease in Jsc, Voc, and PCE of the device are determined by the combined action of the reduction in resistance and shortening of carrier lifetime with the extension of the MAI deposition time.

It must be pointed out that the optimal performance of the device is not the best no matter from the perspective of a single electrochemical parameter, which indicates that the optimization condition of the device is the result of multiple factors. For example, the sample with a MAI a deposition time of 180 s shows the minimum resistance, but it also shows the worst perovskite layer homogeneity.

4. Conclusions

In this work, a series of perovskite layers was successfully manufactured on mesoporous TiO_2 via low-voltage room-temperature electrochemical deposition. In contrast to a similar previously reported method, our proposed method could be easily used, and no high voltage pulse was needed. The morphological characteristics of the manufactured perovskite layer were controllable and could be easily optimized by adjusting the deposition time of Pb and MAI. These perovskite layers were made into mesoporous PSCs. The perovskite layers and solar cells were then analyzed through several characterization methods, and the results revealed that the manufactured perovskite layers could be uniform and could have high coverage. A possible two-step perovskite electrochemical deposition process was presented on the basis of these results.

Declaration of Competing Interest

The authors declare that they have no known competing financial interests or personal relationships that could have appeared to influence the work reported in this paper.

Acknowledgements

This work was supported by National Natural Science Foundation of China (Nos. 61871198, 61474057 and 61520106003), National key Research and Development Program of China (No. 2016YFC0201002), National High-Tech Research and Development Program of China (863 Program, No. 2014AA06A505).

Appendix A. Supplementary material

Supplementary data to this article can be found online at https://doi.org/10.1016/j.solener.2020.11.010.

References

Bi, D., Yi, C., Luo, J., Décoppet, J., Zhang, F., Zakeeruddin, S.M., Li, X., Hagfeldt, A., Grätzel, M., 2016. Polymer-templated nucleation and crystal growth of perovskite films for solar cells with efficiency greater than 21%. Nat. Energy 10, 16142. https://doi.org/10.1038/nenergy.2016.142.

Bunaciu, A.A., Udriştioiu, E.G., Aboul-Enein, H.Y., 2015. X-Ray Diffraction: instrumentation and applications. Crit. Rev. Anal. Chem. 45, 289–299. https://doi.org/10.1080/10408347.2014.949616.

Charles, U.A., Ibrahima, M.A., Teridia, M.A.M., 2018. Electrodeposition of organic–inorganic tri-halide perovskites solar cell. J. Power Sources 378, 717–731. https://doi.org/10.1016/j.jpowsour.2017.12.075.

Chen, M., Ju, M., Garces, H.F., Carl, A.D., Ono, L.K., Hawash, Z., Zhang, Y., Shen, T., Qi, Y., Grimm, R.L., Pacifici, D., Zeng, X., Zhou, Y., Padture, N.P., 2019. Highly stable and efficient all-inorganic lead-free perovskite solar cells with native-oxide passivation. Nat. Commun. 10, 16. https://doi.org/10.1038/s41467-018-07951-y.

Chen, Y., Sun, Y., Peng, J., Tang, J., Zheng, K., Liang, Z., 2018. 2D ruddlesden-popper perovskites for optoelectronics. Adv. Mat. 30, 1703487. https://doi.org/10.1002/adma.201703487.

Correa-Baena, J.P., Saliba, M., Buonassisi, T., Grätzel, M., Abate, A., Tress, W., Hagfeldt, A., 2017. Promises and challenges of perovskite solar cells. Science 358, 739–744. https://doi.org/10.1126/science.aam6323.

de Quilettes, D.W., Vorpahl, S.M., Stranks, S.D., Nagaoka, H., Eperon, G.E., Ziffer, M.E., Snaith, H.J., Ginger, D.S., 2015. Impact of microstructure on local carrier lifetime in perovskite solar cells. Science 348, 683–686. https://doi.org/10.1126/science.aaa5333.

Guerrero, A., Garcia-Belmonte, G., Mora-Sero, I., Bisquert, J., Kang, Y.S., Jacobsson, T.J., Correa-Baena, J., Hagfeldt, A., 2016. Properties of contact and bulk impedances in hybrid lead halide perovskite solar cells including inductive loop elements. J. Phys. Chem. C 120, 8023–8032. https://doi.org/10.1021/acs.jpcc.6b01728.

Han, Y., Meyer, S., Dkhissi, Y., Weber, K., Pringle, J.M., Bach, U., Spiccia, L., Cheng, Y., 2015. Degradation observations of encapsulated planar $CH_3NH_3PbI_3$ perovskite solar cells at high temperatures and humidity. J. Mater. Chem. A 15, 8139–8147. https://doi.org/10.1039/c5ta00358j.

Huang, J., Yuan, Y., Shao, Y., Yan, Y., 2017. Understanding the physical properties of hybrid perovskites for photovoltaic applications. Nat. Rev. Mater. 2, 17042. https://doi.org/10.1038/natrevmats.2017.42.

Jeon, N.J., Na, H., Jung, E.H., Yang, T., Lee, Y.G., Kim, G., Shin, H., Seok, S., Lee, J., Seo, J., 2018. A fluorene-terminated hole-transporting material for highly efficient and stable perovskite solar cells. Nat. Energy 8, 682–689. https://doi.org/10.1038/s41560-018-0200-6.

Kim, H.S., Im, S.H., Park, N.G., 2014. Organolead halide perovskite: new horizons in solar cell research. J. Phys. Chem. C. 118, 5615–5625. https://doi.org/10.1021/jp409025w.

Kojima, A., Teshima, K., Shirai, Y., Miyasaka, T., 2009. Organometal halide perovskites as visible-light sensitizers for photovoltaic cells. J. Am. Chem. Soc. 131, 6050–6051. https://doi.org/10.1021/ja809598r.

Lee, D.S., Seo, S.W., Park, M., Cheon, K.B., Ji, S.G., Park, I.J., Kim, J.Y., 2019. Electrochemical approach for preparing conformal methylammonium lead iodide layer. Electrochem commun 103, 120–126. https://doi.org/10.1016/j.elecom.2019.05.016.

Lee, J., Bae, S., Hsieh, Y., DeMarco, N., Wang, M., Sun, P., Yang, Y., 2017. A bifunctional lewis base additive for microscopic homogeneity in perovskite Solar Cells. Chem 3, 290–302. https://doi.org/10.1016/j.chempr.2017.05.020.

Liu, J., Li, N., Jia, J., Dong, J., Qiu, Z., Iqbal, S., Cao, B., 2019. Perovskite films grown with green mixed anti-solvent for highly efficient solar cells with enhanced stability. Sol. Energy 181, 285–292. https://doi.org/10.1016/j.solener.2019.02.020.

National Renewable Energy Laboratory, 2020. Efficiency chart of solar cells. http://www.nrel.gov/ncpv/images/efficiency_chart.jpg.
Pockett, A., Eperon, G.E., Peltola, T., Snaith, H.J., Walker, A., Peter, L.M., Cameron, P.J., 2015. Characterization of planar lead halide perovskite solar cells by impedance spectroscopy, open-circuit photovoltage decay, and intensity-modulated photovoltage/photocurrent spectroscopy. J. Phys. Chem. C 119, 3456–3465. https://doi.org/10.1021/jp510837q.
Popov, G., Mattinen, M., Kemell, M.L., Ritala, M., Leskelä, M., 2016. Scalable Route to the fabrication of CH3NH3PbI3 perovskite thin films by electrodeposition and vapor conversion. ACS Omega 1, 1296–1306. https://doi.org/10.1021/acsomega.6b00351.
Qiu, L., Ono, L.K., Jiang, Y., Leyden, M.R., Raga, S.R., Wang, S., Qi, Y., 2017. Engineering interface structure to improve efficiency and stability of organometal halide perovskite solar cells. J. Phys. Chem. B 122, 511–520. https://doi.org/10.1021/acs.jpcb.7b03921.
Shin, S.S., Yeom, E.J., Yang, W.S., Hur, S., Kim, M.G., Im, J., Seo, J., Noh, J., Seok, S.I., 2017. Colloidally prepared La-doped BaSnO3 electrodes for efficient, photostable perovskite solar cells. Science 356, 167–171. https://doi.org/10.1126/science.aam6620.
Tai, Q., Tang, K., Yan, F., 2019. Recent progress of inorganic perovskite solar cells. Energy Environ. Sci. 12, 2375–2405. https://doi.org/10.1039/C9EE01479A.
Tan, H., Jain, A., Voznyy, O., Lan, X., de Arquer, F.P.G., Fan, J.Z., Quintero-Bermudez, R., Yuan, M., Zhang, B., Zhao, Y., Fan, F., Li, P., Quan, L.N., Zhao, Y., Lu, Z., Yang, Z., Hoogland, S., Sargent, E.H., 2017. Efficient and stable solution-processed planar perovskite solar cells via contact passivation. Science 355, 722–726. https://doi.org/10.1126/science.aai9081.
Tang, X., Matt, G.J., Gao, S., Gu, E., Almora, O., Brabec, C.J., 2019. Electrical-field-driven tunable spectral responses in a broadband absorbing perovskite photodiode. ACS Appl. Mater. Interfaces 11, 39018–39025. https://doi.org/10.1021/acsami.9b14788.
Wang, S., Li, X., Wu, J., Wen, W., Qi, Y., 2018. Fabrication of efficient metal halide perovskite solar cells by vacuum thermal evaporation: a progress review. Curr. Opin. Electrochem. 11, 130–140.
Yi, C., Luo, J., Meloni, S., Boziki, A., Ashari-Astani, N., Grätzel, C., Zakeeruddin, S.M., Röthlisberger, U., Grätzel, M., 2016. ABX3 metal halide perovskites for high performance perovskite solar cells. Energy Environ. Sci. 9, 656–662. https://doi.org/10.1039/C5EE03255E.
Yi, Luo, J., Meloni, S., Boziki, A., Ashari-Astani, N., Grätzel, C., Zakeeruddin, S.M., Röthlisberger, U., Grätzel, M., 2014. A review on electrical characterization techniques performed to study the device performance of quantum dot sensitized solar cell. J. Am. Chem. Soc. 136, 622–625. https://doi.org/10.1016/j.solener.2017.11.037.
Zhao, Y., Zhu, K., 2014. Solution chemistry engineering toward high-efficiency perovskite solar cells. J. Phys. Chem. Lett. 23, 4175–4186. https://doi.org/10.1021/jz501983v.
Zhou, F., Liu, H., Wang, X., Shen, W., 2017. Fast and controllable electric-field-assisted reactive deposited stable and annealing-free perovskite toward applicable high-performance solar cells. Adv. Funct. Mater. 27, 1606156. https://doi.org/10.1002/adfm.201606156.
Zhou, H., Chen, Q., Li, G., Luo, S., Song, T., Duan, H., Hong, Z., You, J., Liu, Y., Yang, Y., 2014. Interface engineering of highly efficient perovskite solar cells. Science 345, 542–546. https://doi.org/10.1126/science.1254050.
Zhou, Y., Game, O.S., Pang, S., Padture, N.P., 2015. Microstructures of organometal trihalide perovskites for solar cells: their evolution from solutions and characterization. J. Phys. Chem. Lett. 23, 4827–4839. https://doi.org/10.1021/acs.jpclett.5b01843.
Zimmermann, I., Aghazada, S., Nazeeruddin, M.K., 2018. Lead and HTM free stable two-dimensional tin perovskites with suitable band gap for solar cell applications. Angew. Chem. Int. Edit. 58, 1072–1076. https://doi.org/10.1002/ange.201811497.

Further reading

Chen, H., Wei, Z., Zheng, X., Yang, S., 2015. A scalable electrodeposition route to the low-cost, versatile and controllable fabrication of perovskite solar cells. Nano Energy 15, 216–226. https://doi.org/10.1016/j.nanoen.2015.04.025.